research papers

Multi-use high/low-temperature and pressure compatible portable chamber for *in situ* grazing-incidence X-ray scattering studies

Pilar Ferrer,[a,b]* Juan Rubio-Zuazo,[a,b] Catherine Heyman,[c] Fatima Esteban-Betegón[a,b] and Germán R. Castro[a,b]

[a]SpLine, Spanish CRG Beamline at the ESRF, BP 220, 38043 Grenoble Cedex, France, [b]Instituto de Ciencia de Materiales de Madrid-ICMM/CSIC, Cantoblanco, Madrid 28049, Spain, and [c]CAO-DAO, 5 place de Gordes, 38000 Grenoble, France. E-mail: pilar.ferrer-escorihuela@diamond.ac.uk

The multipurpose portable ultra-high-vacuum-compatible chamber described in detail in this article has been designed to carry out grazing-incidence X-ray scattering techniques on the BM25-SpLine CRG beamline at the ESRF. The chamber has a cylindrical form, built on a 360° beryllium double-ended conflate flange (CF) nipple. The main advantage of this chamber design is the wide sample temperature range, which may be varied between 60 and 1000 K. Other advantages of using a cylinder are that the wall thickness is reduced to a minimum value, keeping maximal solid angle accessibility and keeping wall absorption of the incoming X-ray beam constant. The heat exchanger is a customized compact liquid-nitrogen (LN2) continuous-flow cryostat. LN2 is transferred from a storage Dewar through a vacuum-isolated transfer line to the heat exchanger. The sample is mounted on a molybdenum support on the heat exchanger, which is equipped with a BORALECTRIC heater element. The chamber versatility extends to the operating pressure, ranging from ultra-high vacuum ($< 10^{-10}$ mbar) to high pressure (up to 3×10^3 mbar). In addition, it is equipped with several CF ports to allocate auxiliary components such as capillary gas-inlet, viewports, leak valves, ion gun, turbo pump, *etc.*, responding to a large variety of experiment requirements. A movable slits set-up has been foreseen to reduce the background and diffuse scattering produced at the beryllium wall. Diffraction data can be recorded either with a point detector or with a bi-dimensional CCD detector, or both detectors simultaneously. The system has been designed to carry out a multitude of experiments in a large variety of environments. The system feasibility is demonstrated by showing temperature-dependence grazing-incidence X-ray diffraction and conductivity measurements on a 20 nm-thick $La_{0.7}Ca_{0.3}MnO_3$ thin film grown on a $SrTiO_3(001)$ substrate.

1. Introduction

Nowadays, advanced materials with novel physical properties require a detailed understanding of their structure at the atomic level. The trend of studying the materials at nanoscale under real working conditions requires developments of new devices to carry out the experiments. Advanced X-ray techniques available at synchrotron radiation sources are playing a key role in the characterization of thin films, nanostructures, surfaces and interfaces. Therefore, advanced instrumentation to perform X-ray scattering techniques is improving and more sophisticated systems are being developed with the aim of studying real materials under real conditions. Grazing-incidence X-ray scattering (GI-XRS) techniques allow structural and morphological studies on surfaces, thin films and interface materials in a non-destructive way (Robinson, 1986; Feidenhans'l, 1989; Renaud, 1998). Owing to the weak surface signal from these materials, the control of the X-ray penetration depth through the incident angle is essential for atomic structure studies whilst sensitive detectors and a high flux of photons are necessary to carry them out. Together with the detector sensitivity and photon sources, the development of environmental set-ups is constantly improving. Some versatile vacuum chambers for GI-XRS studies have been developed,

attempting to replicate the real working conditions of the applied samples (Carbone *et al.*, 2008, and references therein; Ritley *et al.*, 2001; Bernard *et al.*, 1999; Dennison *et al.*, 1992).

Usually, experiments performed on synchrotron beamlines are carried out under a wide variety of environmental experimental conditions. The crystal structures of insulators, semiconductors and metallic materials of different natures can be studied by GI-XRS as a function of temperature, pressure, gases atmosphere, electric field, *etc.* (Matsui & Mizuki, 1993; Bernard *et al.*, 1999; Fong & Thompson, 2006). In order to include the largest number of experiments possible, a versatile portable ultra-high-vacuum-compatible and high-pressure 'baby chamber' has been designed. The chamber is perfectly suitable for grazing-incidence X-ray diffraction (GIXRD) and grazing-incidence small-angle X-ray scattering (GISAXS) measurements and X-ray reflectivity (XRR) under different environment conditions. The portable ultra-high-vacuum-compatible chamber has been designed to be mounted on the X-ray six-circle multipurpose diffractometer at SpLine, the Spanish CRG BM25 (Branch B) beamline at the European Synchrotron Radiation Facility (ESRF) (Castro, 1998). Moreover, owing to the portable nature of the chamber, it can be mounted in many other end-stations (for example, including those with X-ray absorption set-ups). X-ray diffraction on free surfaces, interfaces, superlattices and thin films can be performed. In this X-ray diffraction end-station, two detectors can be used simultaneously with this portable chamber: a scintillation point detector and a two-dimensional charge-coupled device (2D-CCD). In addition, the chamber allows the installation of ultra-high-vacuum-compatible components, such as evaporators, leak valves, ion guns, *etc.*

The main goals are the capability to work in a wide pressure range going from UHV to 3 bar allowing simultaneously electrical conductivity characterization over a broad temperature range. The chamber incorporates a cooling/heating system to control the sample temperature between 60 K and 1000 K.

In this article we describe a multipurpose chamber designed for the study of surfaces/interfaces/multilayer materials, thin films, in single-crystal form or as compacted powder pellets, by X-ray scattering techniques under different sample environment conditions, highlighting the movable slits for diffuse scattering reduction and the possibility of sample heating/cooling. In order to show the chamber capabilities, an experiment related to the correlation between the transport properties and the atomic structure of oxygen-deficient $La_{0.7}Ca_{0.3}MnO_3$ thin films is presented.

2. Description of the baby chamber

The chamber has a cylindrical form, built on a 360° beryllium nipple, which allows a complete atomic structural characterization under grazing-incidence conditions, as well as *in situ* studies in order to follow, for example, growth processes, phase transitions or structural evolution of thin films or multilayer samples under the effect of an electric field and/or special gases atmosphere.

A real image of the versatile UHV/high-pressure baby chamber ($<10^{-10}$ to $\sim 3 \times 10^3$ mbar) is shown in Fig. 1 (central block). Most parts of the baby chamber are made of stainless steel with the exception of the cryostat and heater parts and Be pipe/windows. Several UHV components (such as, for example, the turbo pump) are located in the upper part of the chamber, leaving a free solid angle of $\sim 1.8\Pi$ sr which corresponds to a polar angle of 51°. The cylinder shape allows the available reciprocal space to be maximized in order to carry out XRR, GIXRD and GISAXS experiments. The dimensions of the whole set-up are kept small enough to allow the diffractometer to work at its full capability maximizing the reciprocal-space accessibility. The chamber, as shown in Fig. 1, is assembled in three separated parts: (*a*) lower body part with eight ports, which contains the continuous-flow cryostat/heater, the sample-holder support and a movable slits system; (*b*) the 360° conflate flange (CF) double-ended Be nipple; and (*c*) two cluster flanges in the upper part with five DN40 CF or seven DN16 CF ports. Fig. 1 shows a series of technical drawings of the baby chamber; the three main parts are displayed in separate drawings and the whole mounted system is also shown.

Two chamber versions can be adopted depending on the experimental needs. Therefore, two different 360° Be-window pipes (CF double-ended nipple) can be used depending on the experiment: (i) double DN100 CF with a Be tube of thickness 0.5 mm, diameter 100 mm and length 150 mm, and (ii) double DN65 CF with a Be tube of thickness 2 mm, diameter 65 mm and length 113 mm. Both configurations allow a maximal vertical scattering angle of 51°. The second configuration has been foreseen to operate at higher pressure; two cluster flanges are available for the upper part, depending on the Be-window pipe used. The main advantages of using a cylinder are firstly that the wall thickness is reduced to a minimum keeping a maximal solid angle accessible for diffracted beams, and secondly that during a θ-scan (azimuthally rotation) the wall absorption of the incoming X-rays is constant. The latter point is of particular importance for correct intensity normalization of diffraction data.

The portable chamber has 15 (or 17) CF ports; ten ports are located in the common lower body part, where eight DN16 CF flanges are foreseen to have electrical feedthroughs for sample heating and/or conductivity measurements and two special liquid-nitrogen (LN2) feedthrough flanges used for continuous cooling liquid circulation. Finally, the two upper cluster flanges with five DN40 CF or seven DN16 CF ports are foreseen for auxiliary components such as capillary gas-inlets, viewports, leak valves, ion gun, turbo pump, *etc.* The CF100 upper-part flange has five DN40 CF ports pointing to the sample position, one in the centre and four distributed at 90° to each other around the central one. These four flanges form a tilt angle of 14.5° with respect to the sample surface normal (see Fig. 1). The flange–sample distance is 258 mm. On the other hand, the CF63 upper part has seven DN16 CF ports, also pointing to the sample position; one is located at the centre and the others regularly distributed at 60° to each other around it. The tilt angle with respect to the surface normal is
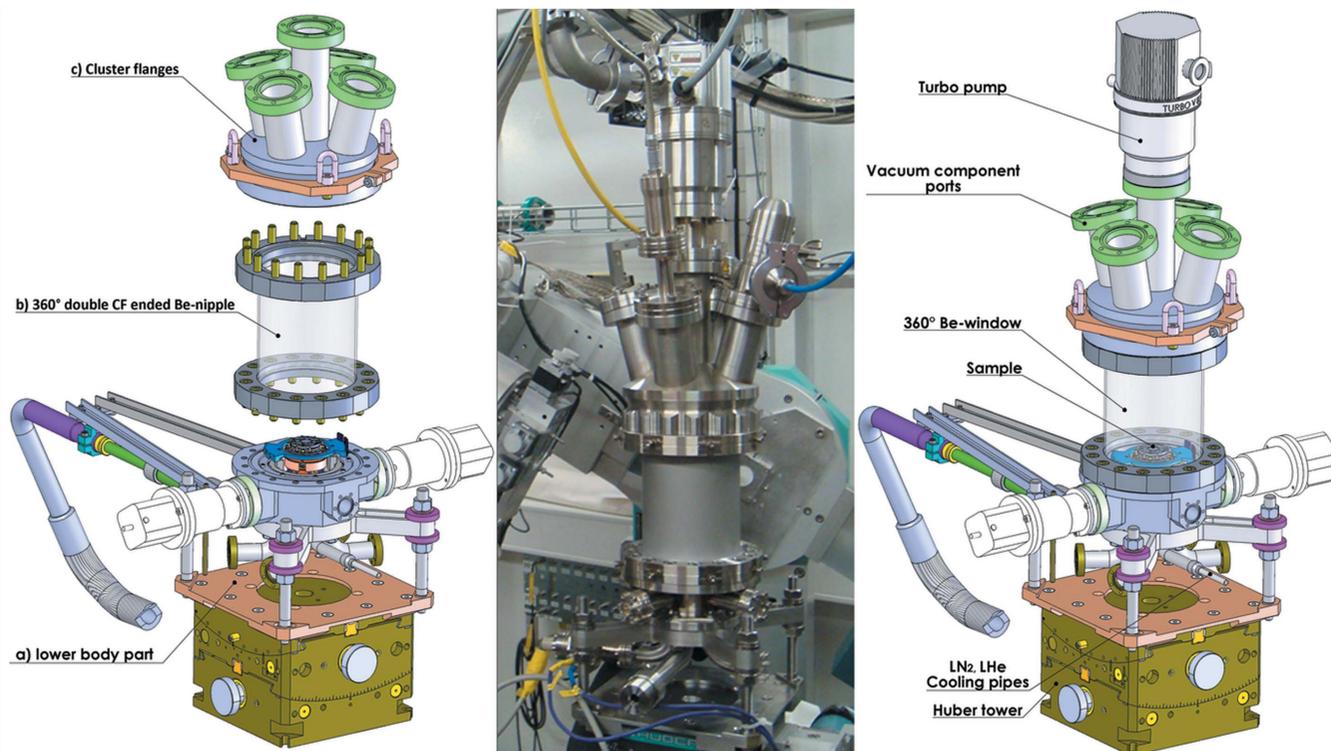
Figure 1
Left: schematic general scheme of the three parts of the portable chamber (see text for details). Centre: photograph of the chamber on the six-circle diffractometer. Right: schematic drawing of the complete portable chamber.

$12°$ and the flange–sample distance is 174 mm. Depending on the experiment requirements, both upper parts can be interchanged by a simple transition tube between the lower body part and the Be-window pipe. In both cases the focal point of the cluster angle ports is the sample position.

Once the equipment is mounted the complete baby chamber dimensions are $\sim$70 cm (or 40 cm depending on the version used) in height, weighing around 20 kg, depending on the configuration required for the experiment.

Three different functionalities have been considered: continuous-flow cryostat control, sample temperature control and sample electrical characterization. In cases where the sample preparation does not require ion bombardment and high environment pressure (up to 3 bar), the second smaller double-ended Be cylinder (DN65 CF, height 89 mm) can be used. In this case the upper part is replaced by a cluster flange with seven DN16 CF flanges.

GIXRD and XRR experiments can be carried out in both configurations as the UHV equipment is positioned in the upper part of the chamber. In the central flange there is usually a turbomolecular pump (Varian TurboV 81-AG), and the others are used for installing other equipment, such us evaporation sources, gas inlets, vacuum gauges, etc. However, if the experimental set-up requires the central flange, the turbo pump can be easily interchanged with other systems.

2.1. Cryostat (common lower part)

The cryostat operation is based on a continuous flow of a cooling liquid [LN2 or liquid helium (LHe)] through the cryostat heat exchanger by pulling the liquid from the Dewar. The cryostat is made using the following components: heat exchanger, storage Dewar, cooled liquid transfer tube, temperature controller and gas flow controller at the outlet pipe. The system is located in the lower part of the portable chamber.

The cooling liquid is drawn from the separate cryogenic storage Dewar, which is maintained at overpressure, and circulated *via* a flexible transfer tube through to the cryostat heat exchanger. The liquid flow can be regulated by a flow valve on the outlet tube. Both the liquid outlet pipe and the transfer tube are flexible allowing the rotation of the cryostat and the baby chamber with respect to the Dewar, and consequently the sample may be positioned with respect to the incoming X-ray beam, making GI-XRS experiments available.

The cryostat incorporates an extended surface heat exchanger (four expansion chambers) at the cold copper block tip which provides efficient heat transfer between the cooling liquid and the sample holder. The liquid flows through this heat exchanger and, as the latent heat of vaporization cools the sample holder, the liquid evaporates and the gas continues to flow through the heat exchanger. All components are made of stainless steel, with the exception of the main heat exchanger, which for thermal reasons is made of oxygen-free copper. Figs. 2 and 3 show two cuts through the cryostat from which it is possible to identify most of the components. The temperature is controlled by either regulating the cooling liquid flux through the heat exchanger or by resistive heating of the exchanger keeping a constant liquid flux. The cooling pipe is designed to be used with LN2 but, if lower temperature
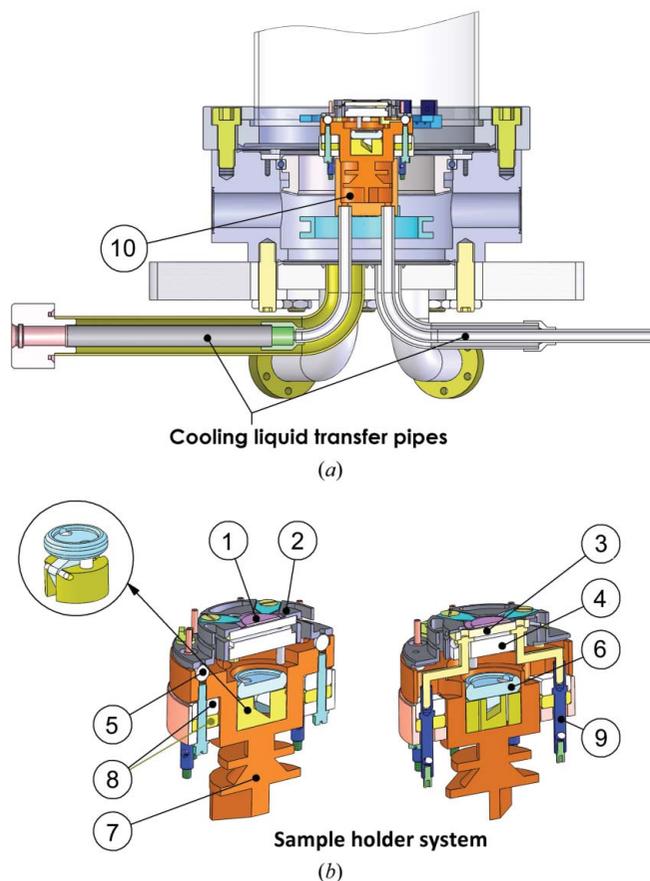
Figure 2
(*a*) Schematic view of the sample holder support. (*b*) Cross section of the sample holder. 1: sample; 2: Mo hat; 3: ceramic heater; 4: isolated ceramic; 5: sapphire balls; 6: push heater piece, detailed in the inset detailed; 7: Cu body; 8: semi-cylindrical ceramics; 9: pins cable connections; 10: gas expansion interior cavity.

is required, LHe can be used. Thus, the sample temperature ranges between 60 and 1000 K or 100 and 1000 K, depending of the liquid used. Temperature control of the continuous-flow cryostat is achieved by a combination of the manual flow control of the liquid (LN2 or LHe) and a resistive electrical heater power control, which is in contact with the heat exchanger. The temperature is monitored by a Pt100, a type K (chrome–nickel and aluminium–nickel) and/or N-type (nicrosil–nisil) temperature sensor attached to the sample holder plate and to the sample. The heat exchanger has an obstructed passage in various steps in order to increase the contact surface between the cooling liquid and the exchanger.

The cooling power and consequently the minimum achievable temperature depends on the cooling liquid used, the sample holder material and the gas mass flow. The cryostat has been designed to be used with LN2 as flowing liquid and radiation shields have not been included. However, in special cases when temperatures lower than 100 K are required, a special small transition inlet tube has been designed. This tube allows the use of LHe. A special support is also added to fix the LHe transfer siphon. Owing to heat losses, the lowest possible sample temperature is 60 K. The sample is fixed on a metal plate which is in thermal contact with the heat

exchanger *via* four sapphire spheres. The sample temperature follows the temperature of the heat exchanger. The stability and fine control of the sample temperature is achieved by an additional heater in direct contact with the sample support plate that allows heating the sample quickly.

2.2. Sample holder

The sample holder has been designed to perform surface studies, from the growing process to diffraction measurements of the sample. Therefore, a robust, very stable and versatile sample holder is required. Specifically, for sample preparation it is often necessary to carry out a combination of sample heating under UHV vacuum conditions and noble-gas ion bombardment. In addition, many experiments require low temperatures. Finally, grazing-incidence diffraction measurements require the sample to be well fixed in position in order to have precise control of the incident angle. Moreover, our design allows the capability to perform electrical transport characterization simultaneously.

Our system foresees the need of separate sample heating, keeping the continuous-flow cryostat at low temperature. The sample temperature is controlled by an extra temperature sensor fitted at the sample position using an additional power dissipation device. The sample is fixed to a molybdenum (or Inconnel) plate in hat form, which is in contact with a ceramic heater (ShinEtsu BORALECTRIC heater elements) in the back (see Fig. 2). In the centre of the Mo (or Inconnel) support the sample is located at the middle of the plate, allowing tilting of the sample with a very low incidence angle, and keeping the sample surface free. The support has some grooves that allow the sample fixation, as well as the thermocouples and/or other electrical components, to be kept without blocking the incident X-ray beam and eliminating any possible sample shadowing. The sample is fixed by means of four (or two) clamps of different dimensions which may be adapted for different sample sizes. Contact between the molybdenum (or Inconnel) plate and the cryostat heat exchanger is made *via* four sapphire balls. The sapphire balls provide the necessary electrical isolation. Moreover, sapphire has excellent thermal conductivity, better than copper, at low temperatures. However, at high temperatures sapphire has poor thermal conductivity, thus avoiding excessive heating of the heat exchanger during the sample heating (see Fig. 2). All these features are, of course, necessary to achieve the temperature requirements and maintain the possibility of polarizing the sample. Two electrical multi-pin feedthroughs are used to provide the necessary electrical contacts for different sample characterization techniques, such as, for example, electrical transport measurements, four-point conductivity measurements, sample polarization voltage, total neutralization (total electron yield), current measurements, *etc.*

As is mandatory in X-ray diffraction, the sample must be rigidly fixed to the diffractometer; therefore, the whole system is mounted on a six-circle diffractometer through a rigid support system consisting of a special adapted fixation plate which has four M16 screws connected/joined to a solid cross-

arm bracket fixed to the lower body part of the chamber. The baby chamber is perfectly fixed on the six-circle diffractometer by a crosshead, as show in Figs. 1 and 2. As it is mounted using a simple screw system, it can be easily installed on other end-stations.

2.3. Chamber adaption

This portable chamber has been designed to carry out a large variety of X-ray scattering experiments with point and/or bi-dimensional detectors. Hence the chamber is suitable for both standard GIXRD and GISAXS, taking advantage of the 2D-CCD detector. However, a drawback could be the presence of additional background and diffuse signal produced by X-ray interaction with the Be walls. The Be reflections produced by the direct incoming and outgoing X-ray beam could present and be an important interference problem, since the scattering signal from surfaces and interfaces is very small in comparison with the intense direct incidence X-ray beam. The beam can produce strong scattering signal at the Be walls and could be a strong drawback since it can overlap the real sample reflections. Thus, this effect has to be taken into account and minimized as much as possible. In general, this effect is neglected when using a point detector since it can be minimized by taking advantage of the set of double slits (as is usual in many detector systems) that reduce the observed solid angle by cutting the contribution from the Be walls. However, for GISAXS this solution presents a drawback owing to the long acquisition time required. In order to profit from the 2D-CCD detector, which reduces considerably the acquisition time, the diffuse scattering produced at the Be window must be reduced or extinguished. Therefore, we have developed a motorized slits system which blocks the diffuse scattering produced by the direct incoming beam and includes a support for a beam stopper inside the chamber (Fig. 3). There are two independent motorized movements: a rotation around the chamber main axis and a vertical translation in the chamber main axis direction. The rotation is produced by means of gear wheels controlled from outside by a rotation feedthrough. The vertical translation is achieved by a cam system using an eccentric rotation feedthrough axis. The eccentric cam is linked to a ring groove which is fixed through two spindle rods. The cam system permits the vertical position to be maintained while the rotation is realised. This mechanism allows the slits to be aligned during data acquisition. The slits' aperture is placed inside, less than 1 mm from the Be walls. The position of the slits is aligned with respect to the direct incoming beam by means of the two independent move-

ments. The slits are kept aligned during data collection by rotating them synchronically in the opposite θ rotation direction (baby chamber). The slits' support has enough space for three different apertures, of diameter 0.5, 1 and 2 mm. The slits are made of molybdenum and are 2 mm thick. Different aperture and thickness dimensions can be mounted if required.

3. Beamline set-up

X-ray diffraction measurements have been carried out at Branch B of the Spanish CRG SpLine-BM25 beamline at the ESRF (Castro, 1998), but the portable character of the chamber itself allows it to be used at different stations. The photon energy of the beamline ranges from 5 to 35 keV (wavelength 2.48 to 0.35 Å) with an energy resolution of $\Delta E/E = 1.4 \times 10^{-4}$. Owing to the high photon flux of the beamline (5×10^{11} photons s^{-1}), surface structure diffraction experiments are possible. The portable vacuum-compatible chamber has been specially conceived to be mounted on the Huber tower placed in a vertical geometry on the six-circle multipurpose diffractometer, taking advantage of the exceptional experimental set-up. A scintillation point detector is mounted on the diffractometer arm for high-resolution experiments; a θ–2θ set-up together with a goniometer head is installed on the detector arm in order to use a crystal analyzer. In addition, a 2D-CCD (Photonic Science) detector is placed on a decoupled motorized stage.

Depending on the experiment requirements, the chamber can be equipped with different components, allowing a wide variety of studies. Crystalline samples, materials submitted to specific treatments, solid–solid phase transitions, reconstruction surfaces, the effect of Ar ions on a sample surface, and growth of high-quality epitaxial layers by MBE or CVD are
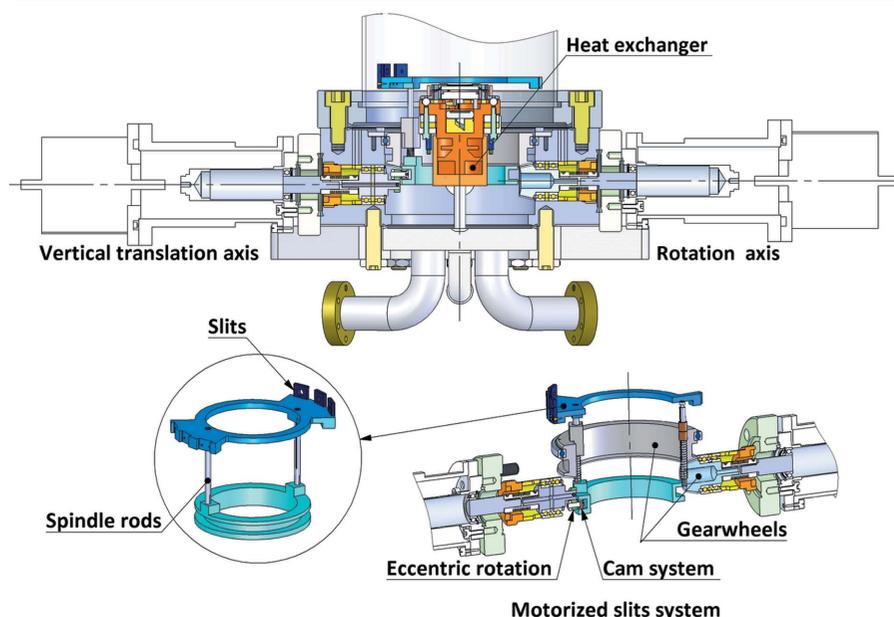

Figure 3
Schematic general scheme of the monitored slits sited in the interior of the chamber.

some of the examples that can be followed *in situ* by both detectors. On this multipurpose diffractometer the CCD detector is used to reduce the data acquisition time and time-resolved experiments (Ferrer *et al.*, 2012). On the other hand, the point detector is used when high resolution is required. Moreover, X-ray small-angle diffraction can be followed with the CCD detector and a specific reciprocal-space area by the point detector simultaneously.

4. Experimental test and validation

The baby chamber has been used in a wide variety of users' experiments demonstrating its high performance (Abad *et al.*, 2012; Alberca *et al.*, 2011; Jarrier *et al.*, 2012; see also http://www.esrf.fr/UsersAndScience/Experiments/CRG/BM25/userinformation/beamtimeschedule_). However, in order to highlight the performance and capability of the present baby chamber system we report in this section a combined electrical transport characterization and grazing-incidence X-ray diffraction experiment carried out on a 20 nm-thick $La_{0.7}Ca_{0.3}MnO_3$ (LCMO) thin film grown on a $SrTiO_3(001)$ (STO) substrate. The results shown here do not pretend to be exhaustive and have only a demonstrative character of the system's capability. These measurements are part of more ambitious research goals concerning the correlation of electrical and magnetic transport properties and atomic structure of perovskite complex oxide thin films.

GIXRD measurements were performed with a monochromatic X-ray beam, set to an energy of 15 keV (wavelength 8.265 nm) and with a spot size of 500 µm × 500 µm. The LCMO film was grown by pulsed laser deposition using a solid-state Nd:YAG laser (model YG 960 from QUANTEL), operated at 355 nm wavelength, 10 Hz and 1 J cm^{-2} irradiance power. The films were grown directly on the STO(001) substrate under an O_2 pressure of 2 mbar. In order to avoid oxygen deficiency, a post-annealing at 1000 K for 40 min was made in a continuous flux of oxygen at atmospheric pressure. A stoichiometric polycrystalline LCMO target was used.

LCMO is a manganite complex oxide which exhibits exotic behaviour such as superconductivity, colossal magnetoresistance, charge ordering, ferroelectricity or multiferroicity. The growth of this material in a thin-film form usually modifies its intrinsic properties. The film thickness plays an important role on the Curie and metal-to-insulator (TMI) transition temperatures (de Andrés *et al.*, 2003). The different magnetic behaviour of the thin films compared with the bulk is generally associated with a mechanism related to the presence of the substrate–layer interface (Fontcuberta *et al.*, 1996; Koo *et al.*, 1997; Sun *et al.*, 1999; Jo *et al.*, 2000; Lu *et al.*, 2000; Rubio-Zuazo *et al.*, 2005). Previous work reveals changes in the crystallographic structure depending on the LCMO thin-film thickness (de Andrés *et al.*, 2003; Rubio-Zuazo *et al.*, 2005). In this example we report the evolution of the atomic structure, as well as the transport properties related to the oxygen vacancies on a 20 nm-thick LCMO thin film.

The sample was installed inside the portable vacuum chamber on the six-circle diffractometer at BM25-B. The atomic structure of the film was followed *in situ* during the heating/deoxygenation process. The sample was heated up to 725 K for 5 h in the portable chamber and the chamber pressure rose to a maximum of 10^{-7} mbar. The incident angle used was $\alpha = 0.5°$ in order to maximize the surface signal. The diffraction datasets of the sample as-grown and after 5 h of heating were obtained at room temperature. For the conductivity measurements the four-point probe method was used. In this method a four-wire electrode is in contact with the sample, using separate electrode pairs for current-carrying and voltage-sensing. The advantage of four-terminal sensors is that the separation of current and voltage electrodes eliminates the impedance contribution of the wiring and contact resistances. Ag-paint glued electrodes pairs were placed in contact with the top plane of the LCMO film. The transport measurements were realised before and after each heating treatment (deoxygenation process). For the measurement a Keithley's Source Meter model 2400 was used. After each transport measurement the sample was cleaned with acetone and then the chamber was pumped down to continue with the sample X-ray diffraction characterization.

The LCMO ideal bulk structure is an orthorhombic distorted perovskite described by the *Pbnm* space group. The epitaxial LCMO thin films adopt a contracted tetragonal lattice symmetry imposed by the STO substrate with the in-plane crystallographic axis rotated by 45° with respect to the substrate crystallographic axis. The in-plane LCMO lattice parameters a and b match the substrate STO, giving rise to a square lattice, as $a_{LCMO} \simeq b_{LCMO} \simeq 2^{1/2}a_{STO}$ and $c_{LCMO} \simeq 2a_{STO}$. A reduction of the out-of-plane lattice parameter ($c = 7.66$ Å) compared with the bulk is also obtained. Since the LCMO in-plane and out-of-plane lattice dimensions are, respectively, $2^{1/2}$ and 2 times those from STO and rotated by 45° on the *c*-axis with respect to the substrate, the manganite shows diffraction peaks at half-integer h, k and l values (with reference to the STO lattice). Therefore the fractional diffraction peaks are produced only by the LCMO film. The thin-film thickness was obtained from X-ray reflectivity measurements (not shown here) and the domain size is deduced from the FWHM of the out-of-plane diffracted peaks of the film, in the half-integer reflections. In the case of the as-grown LCMO film, the analysis of the diffraction data, shown in Fig. 4, reflects a bulk-like structure with a *Pbnm* space group, as is expected for a fully oxygenated sample. In addition, the transport properties support the presence of the bulk structure (Fig. 5).

Once the sample is heated, the diffraction data show dramatic modifications in the peak intensities implying significant changes in the manganite crystalline structure (Fig. 4). The intensity ratio between the diffracted peaks for the as-grown and heated films differ considerably as can be clearly seen in the representative out-of-plane scans along the $(1\,1\,l)$-CTR, $(1.5\,0.5\,l)$-rod and $(1.5\,1.5\,l)$-rod shown in Fig. 4. Remarkably, we observe a loss of intensity on the half-integer *l*-reflections with integer h and k values, and on the integer *l*-reflections with half-integer h and k values. The structure factors for these reflections are very sensitive to the distortions
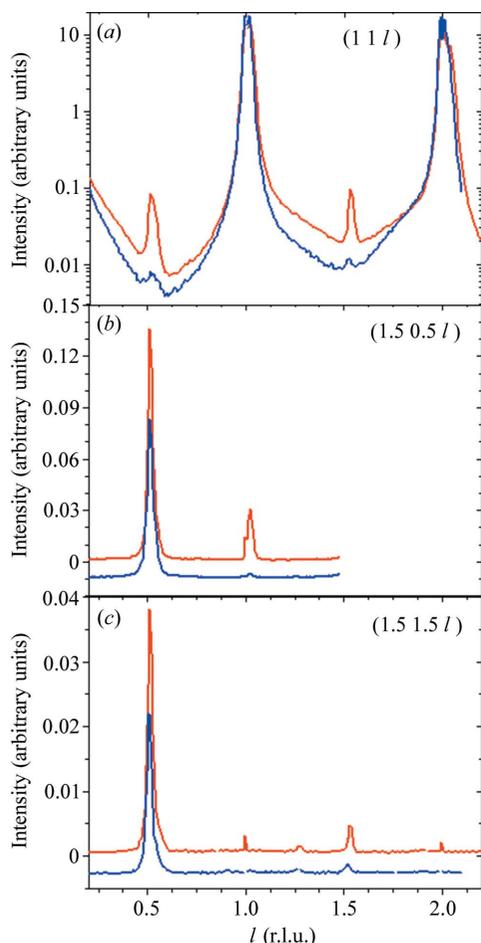
Figure 4
Crystal truncation rods $(1\,1\,l)$, $(1.5\,0.5\,l)$ and $(1.5\,1.5\,l)$ of LCMO/STO(001) for the as-grown sample [grey (red online)] and 5 h of annealing at 725 K [black (blue online)] under high-vacuum conditions. h, k and l values refer to the STO lattice parameters.

Figure 5
Transport measurements for the as-grown sample [grey (red online)] and after 5 h of annealing at 725 K [black (blue online)] under high-vacuum conditions.

of the MnO$_6$ block basal plane and to the positions of the La/Ca atoms, while the structure factors for the rest of the reflections are sensitive to the position of the apical O atoms (de Andrés *et al.*, 2003; Rubio-Zuazo *et al.*, 2005; International Tables for Crystallography, 2005). Hence, the diffraction patterns are compatible with an atomic structure model in which the La and Ca ions tend to remain at the regular position of the perovskite and the octahedral basal plane tends to be coplanar, aligning the Mn—O—Mn bonding (180° angle) between adjacent MnO$_6$ blocks. However, a cooperative displacement of the apical O atoms is still present preserving the double lattice parameter. The transport measurements show a drastic decrease of the TMI temperature from 265 K for the as-grown sample to 170 K for the heated sample (Fig. 5). Although the atomic structure of the oxygen-deficient sample enhances the double exchange mechanism, the lack of oxygen ions preserves considerably the electron hopping from Mn^{3+} to Mn^{4+} (*via* the missing oxygen) reducing the TMI transition temperature and increasing the film resistivity. Hence, the present study demonstrates that, although the Mn octahedral distortions play a key role in the
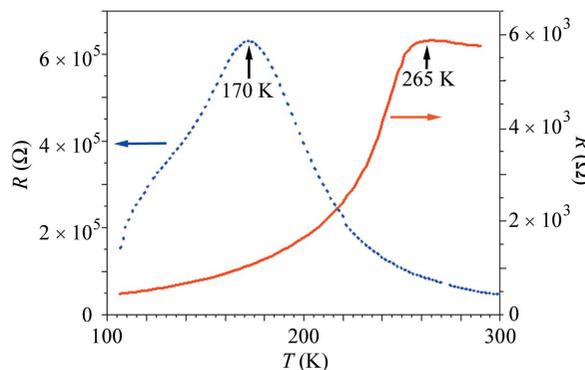
transport properties of manganites-based films, the major subject of many research studies, the oxygen deficiency is the main cause for the decrease of the TMI.

5. Conclusions

In this article a multipurpose portable vacuum-compatible chamber designed to carry out grazing-incidence X-ray scattering measurements has been described. Experiments on surfaces/interfaces/multilayer materials, thin films, single crystals or compacted powder pellets in a large variety of environments and experiments to follow the growth or evolution of the sample *in situ* can be performed. The sample temperature ranges from 60 to 1000 K, as the cryosystem can work with both liquid He and N$_2$. The pressure range goes from 3 bar to $\sim 10^{-10}$ mbar.

The chamber feasibility has been demonstrated by a study of the role of the oxygen vacancies on the atomic structure and transport properties of a 20 nm-thick LCMO thin film on a STO(001) substrate. The diffraction data, heating process and transport measurements carried out during the experiment have been performed on the portable chamber.

References

Abad, J., Espinosa, N., Ferrer, P., García-Valverde, R., Miguel, C., Padilla, J., Alcolea, A., Castro, G. R., Colchero, J. & Urbina, A. (2012). *Sol. Energy Mater. Sol. Cells*, **97**, 109–118.
Alberca, A., Nemes, N. M., Mompean, F. J., Biskup, N., de Andres, A., Munuera, C., Tornos, J., Leon, C., Hernando, A., Ferrer, P., Castro, G. R., Santamaria, J. & Garcia-Hernandez, M. (2011). *Phys. Rev. B*, **84**, 134402.
Andrés, A. de, Rubio, J., Castro, G., Taboada, S., Martínez, J. L. & Colino, J. M. (2003). *Appl. Phys. Lett.* **83**, 713.
Bernard, P., Peters, K., Alvarez, J. & Ferrer, S. (1999). *Rev. Sci. Instrum.* **70**, 1478.

Carbone, D., Plantevin, O., Gago, R., Mocuta, C., Bikondoa, O., Alija, A., Petit, L., Djazuli, H. & Metzger, T.-H. (2008). *J. Synchrotron Rad.* **15**, 414–419.

Castro, G. R. (1998). *J. Synchrotron Rad.* **5**, 657–660.

Dennison, J. R., Wang, S., Dai, P., Angot, T., Taub, H. & Ehrlich, S. N. (1992). *Rev. Sci. Instrum.* **63**, 3835.

Feidenhans'l, R. (1989). *Surf. Sci. Rep.* **10**, 105–188.

Ferrer, P., da Silva, I., Rubio-Zuazo, J., Alfonso, B. F., Trobajo, C., Khainakov, S., Garcia, J. R., Garcia-Granda, S. & Castro, G. R. (2012). *J. Synchrotron Rad.* **19**, 93–100.

Fong, D. D. & Thompson, C. (2006). *Annu. Rev. Mater. Sci.* **36**, 431–465.

Fontcuberta, J., Martínez, B., Seffar, A., Piñol, S., García-Muñoz, J. L. & Obradors, X. (1996). *Phys. Rev. Lett.* **76**, 1122–1125.

International Tables for Crystallography (2005). *International Tables for Crystallography*, Vol. A, ch. 7.1, p. 276. Heidelberg: Springer.

Jarrier, R., Marti, X., Herrero-Albillos, J., Ferrer, P., Haumont, R., Gemeiner, P., Geneste, G., Berthet, P., Schülli, T., Cevc, P., Blinc, R., Wong, S. S., Park, T.-J., Alexe, M., Carpenter, M. A., Scott, J. F., Catalan, G. & Dkhil, B. (2012). *Phys. Rev. B*, **85**, 184104.

Jo, M., Mathur, N., Todd, N. & Blamire, M. (2000). *Phys. Rev. B*, **61**, R14905–R14908.

Koo, T. Y., Park, S. H., Lee, K. & Jeong, Y. H. (1997). *Appl. Phys. Lett.* **71**, 977.

Lu, C. J., Wang, Z. L., Kwon, C. & Jia, Q. X. (2000). *J. Appl. Phys.* **88**, 4032.

Matsui, J. & Mizuki, J. (1993). *Annu. Rev. Mater. Sci.* **23**, 295–320.

Renaud, G. (1998). *Surf. Sci. Rep.* **32**, 1–90.

Ritley, K. A., Krause, B., Schreiber, F. & Dosch, H. (2001). *Rev. Sci. Intrum.* **72**, 1453.

Robinson, I. (1986). *Phys. Rev. B*, **33**, 3830–3836.

Rubio-Zuazo, J., de Andrés, A., Taboada, S., Prieto, C., Martínez, J. & Castro, G. (2005). *Physica B*, **357**, 159–164.

Sun, J. Z., Abraham, D. W., Rao, R. A. & Eom, C. B. (1999). *Appl. Phys. Lett.* **74**, 3017.